



One-dimensional model of manifold microchannels for embedded cooling: Prediction of thermal performance and flow non-uniformity

Hansol Lee¹, Young Jin Lee¹, Sung Jin Kim^{*}

Department of Mechanical Engineering, Korea Advanced Institute of Science and Technology, 291 Daehak-ro, 34141 Daejeon, Republic of Korea



ARTICLE INFO

Keywords:
 Embedded cooling
 Manifold microchannels
 Power electronics
 High heat flux cooling
 Thermal management
 Flow non-uniformity

ABSTRACT

A one-dimensional model has been developed to accurately predict the thermal performance and flow non-uniformity of the manifold microchannels (MMC) for embedded liquid cooling. The model consists of one-dimensional governing equations derived from the integral relations of momentum and energy over appropriately-defined two separate control volumes. To validate the model, a series of 3-D numerical simulation is conducted over the wide ranges of the Reynolds number ($Re_{m,in}$) at the manifold inlet from 560 to 3190, the dimensionless hydraulic flow length (x^+) from 0.012 to 0.123, and the dimensionless thermal flow length (χ^*) from 0.002 to 0.023. It is shown that the model provides accurate predictions of the thermal performance and flow non-uniformity (CV) of MMC heat sinks within the root mean square percentage error (RMSPE) of 6% and 26% for 50 data points, respectively. The significant improvement of the prediction accuracy is made over the earlier models with an error reduction of 82%. Finally, a design guideline for the uniform flow distribution is suggested for the first time based on a newly proposed explicit correlation for predicting the flow non-uniformity: the dynamic pressure at the manifold inlet should be kept smaller than the pressure drop across the microchannels.

1. Introduction

The electrification of the automobile industry and the advancement in the grid systems to mitigate the environmental and energy concerns have led to an increase in the demands for high-power-density power modules, particularly based on wide band gap (WBG) semiconductors such as gallium nitride (GaN) and silicon carbide (SiC) [1–3]. Due to the increase in the power density of these electronics, the die-level heat flux of the electronics is even projected to reach over 1 kW/cm² [4,5]. While these power electronics enable operation at higher voltage and switching frequencies compared to the conventional silicon based power electronics, their performance has been constrained by challenges in thermal management [6,7]. Therefore, it is an urgent challenge to develop effective cooling solutions which can alleviate the thermal issues within the high heat-flux electronics. Earlier studies have shown that embedded microchannel liquid cooling can be an effective cooling scheme for such high heat-flux electronics. However, conventional microchannel cooling suffers from a high pressure drop and a significant temperature difference across a chip surface [8–11]. To overcome these major drawbacks, the concept of manifold microchannel (MMC) heat sink has been proposed,

and it has been experimentally [12–25] and numerically [26–36] investigated. An MMC heat sink distinguishes itself from a conventional microchannel heat sink by having an additional fluid-distributing manifold bonded on top of the microchannels. Since the overlying manifold distributes the fluid through a slot jet array, a flow length within the microchannels becomes very short compared to the overall size of a chip — typically one-tenth of the chip length. Therefore, an MMC heat sink can yield relatively low pressure drop and mitigated temperature difference across the chip surface, making them a promising solution for thermal management of high heat-flux electronics.

To implement an MMC heat sink for thermal management of various industrial applications, it is essential to predict the thermal performance with respect to its geometric parameters and operating conditions. For this, theoretical models have been developed based on the assumption of the uniform flow distribution among the microchannels for simplicity of analysis [13–15,20,37]. However, Copeland et al. [13] have shown that their model exhibits a large discrepancy of over 100% in predicting the thermal resistance of an MMC heat sink compared to the experimental data, which raises doubts about the validity of the assumption. Results from the recent numerical and experimental studies support that the main fluid stream within the manifold is unevenly distributed to the

* Corresponding author.

E-mail address: sungjinkim@kaist.ac.kr (S.J. Kim).

¹ These authors contributed equally to this work.

Nomenclature	
$A_{b,y}$	Cross-sectional area of the substrate base of the solid control volume perpendicular to the y direction ($= 2L_{unit}t_b$) [m 2]
$A_{b,z}$	Cross-sectional area of the substrate base of the solid control volume perpendicular to the z direction ($= 2L_{unit}\Delta y$) [m 2]
A_c	Cross-sectional area of the microchannel ($= w_c H_c$) [m 2]
$A_{c,in}$	Cross-sectional area of the microchannel inlet ($= L_{in}w_c$) [m 2]
$A_{c,out}$	Cross-sectional area of the microchannel outlet ($= L_{out}w_c$) [m 2]
$A_{m,in}$	Cross-sectional area of the manifold inlet ($= L_{in}H_m$) [m 2]
$A_{m,out}$	Cross-sectional area of the manifold outlet ($= L_{out}\Delta y$) [m 2]
c_p	Fluid heat capacity [J/kg-K]
D_c	Hydraulic diameter of the microchannel ($= \sqrt{A_c}$) [m]
$D_{c,in}$	Hydraulic diameter of the microchannel inlet ($= \sqrt{A_{c,in}}$) [m]
$D_{c,out}$	Hydraulic diameter of the microchannel outlet ($= \sqrt{A_{c,out}}$) [m]
D_m	Hydraulic diameter of the manifold inlet conduit ($= \sqrt{A_{m,in}}$) [m]
$\Delta P_{c,f}$	Frictional pressure drop across the microchannels [Pa]
ΔP_{minor}	Minor pressure loss [Pa]
$\Delta P_{m,out}$	Frictional pressure drop across the manifold outlet conduit [Pa]
Δy	Microchannel spacing ($= w_c + t_c$) [m]
f_c	Friction factor within the microchannel
f_m	Friction factor within the manifold inlet conduit
$f_{m,out}$	Friction factor within the manifold outlet conduit
H_c	Height of the microchannel [m]
H_m	Height of the manifold inlet conduit [m]
\bar{h}	Average heat transfer coefficient [W/m 2 -K]
K_c	Contraction loss coefficient
K_e	Expansion loss coefficient
K_{minor}	Minor loss coefficient
$K_{90,in}$	90-deg bend loss coefficient at the microchannel inlet
$K_{90,out}$	90-deg bend loss coefficient at the microchannel outlet
k_f	Fluid thermal conductivity [W/m-K]
k_s	Solid thermal conductivity [W/m-K]
L_{chip}	Chip length [m]
L_{flow}	Flow length within the microchannels ($= L_{in}/4 + t_m + L_{out}/4$) [m]
L_{in}	Width of the manifold inlet [m]
L_{out}	Width of the manifold outlet [m]
$L_{p,c}$	Perimeter of the microchannel ($= w_c + 2H_c$) [m]
$L_{p,m,in}$	Perimeter of the manifold inlet ($= L_{in} + 2H_m$) [m]
$L_{p,m,out}$	Perimeter of the manifold outlet ($= 2\Delta y$) [m]
L_{plenum}	Length of the manifold inlet plenum [m]
L_{unit}	Length of the unit cell ($= L_{in}/2 + t_m + L_{out}/2$) [m]
\dot{m}_c	Channel mass flow rate [kg/s]
$P_{m,out}$	Static pressure at the manifold outlet [Pa]
Pr	Prandtl number
q''	Heat flux [W/cm 2]
Re_c	Channel Reynolds number ($= \frac{V_c D_c}{\nu}$)
Re_m	Manifold Reynolds number ($= \frac{UD_m}{\nu}$)
$Re_{m,in}$	Reynolds number at the manifold inlet ($= \frac{U_{in}D_m}{\nu}$)
\bar{T}	Temperature at the center of the solid control volume [°C]
T_{in}	Fluid inlet temperature [°C]
T_{out}	Fluid outlet temperature [°C]
t_b	Substrate base thickness [m]
t_c	Thickness of the microchannel fin [m]
t_m	Thickness of the manifold wall [m]
$t_{w,c}$	Thickness of the microchannel wafer [m]
$t_{w,m}$	Thickness of the manifold wafer [m]
w_c	Width of the microchannel [m]
x^+	Dimensionless hydraulic flow length = $\left(\frac{L_{flow}}{Re_c D_c} \right)$
x^*	Dimensionless thermal flow length = $\left(\frac{L_{flow}}{Re_c D_c Pr} \right)$
A_{tot}	Total wetted surface area of a single unit cell ($= (w_c + 2H_c + t_c)L_{flow}$) [m 2]
AR	Aspect ratio of the microchannel ($= H_c/w_c$)
\dot{m}_c	Channel mass flow rate ($= \rho A_{c,in} V_{c,in}$) [m 2]
N_m	The number of manifold channels
T_b	Base temperature adjacent to the fluid flow (Eq. (24)) [°C]
T_f	Bulk mean fluid temperature (Eq. (25)) [°C]
U	Average velocity of the main fluid stream in the y direction [m/s]
$U_{c,in}$	Average velocity of the branching flow in the y direction at the microchannel inlet (Eq. (9)) [m/s]
U_{in}	Average velocity at the manifold inlet ($= \frac{\dot{V}_m}{2A_{m,in}}$) [m/s] [m/s]
V_c	Average velocity of the flow within the microchannel ($= \left(\frac{A_{m,in}}{2A_c} \right) \left(\frac{L_{chip}}{2n} \right) \frac{dU}{dy}$) [m/s]
$V_{c,in}$	Average velocity of the branching flow in the $-z$ direction (Eq. (7)) [m/s]
$V_{m,out}$	Average velocity at the manifold outlet (Eq. (13)) [m/s]
\dot{V}	Total volume flow rate [m 3 /s]
\dot{V}_m	Total volume flow rate within a single manifold channel ($= \frac{\dot{V}}{N_m}$) [m 3 /s]
<i>Greek letters</i>	
γ	Static pressure regain coefficient
ρ	Fluid density [kg/m 3]
τ_w	Average wall shear stress [Pa]
<i>Subscripts</i>	
c	Microchannel
in	Inlet
m	Manifold
out	Outlet
w	Wafer

microchannels, and the thermal-hydraulic performance of an MMC heat sink is significantly affected by the uneven flow distribution [37,38]. Boteler et al. [37] reported that the flow rate in each microchannel deviates by a factor of six depending on the manifold geometry and the total flow rate, which implies that the assumption of the uniform flow distribution among the microchannels may not be justified in general. Jung et al. [38] experimentally showed that a difference of over 10 K between the maximum and the average temperatures of $5 \times 5 \text{ mm}^2$ chip exists at the heat flux of 250 W/cm^2 , due mainly to the non-uniform flow distribution. These results suggest that the non-uniform flow distribution and its effect on the temperature distribution should be taken into account to accurately predict the thermal performance of an MMC heat sink.

In this study, a theoretical model of an MMC heat sink is introduced. The proposed model provides a systematic perspective to analyze the thermal performance and the flow non-uniformity of the MMC heat sink. The model consists of one-dimensional momentum and energy equations. These two one-dimensional governing equations are derived from integral relations of momentum and energy over appropriately-defined two separate control volumes. Specifically, a control volume for the momentum balance is defined in the fluid region, including a dividing flow junction where the main fluid stream branches off from the manifold to the microchannels. A control volume for the energy balance in the solid region is defined so that it incorporates an individual microchannel and its solid substrate. The formulation of the specific control volumes allows the transformation of the governing partial differential equations into the one-dimensional governing equations in the form of ordinary differential equations. After deriving the one-dimensional governing equations, the flow distribution among the microchannels and the resultant temperature distribution within the solid substrate are estimated by solving these equations. To validate the proposed model, an extensive parametric study is performed for a wide range of geometric parameters and operating conditions using 3-D numerical simulation which is validated by the previous experimental data. The total thermal resistance and the coefficient of variation (CV) of the flow distribution predicted by the present model are compared with the 3-D numerical dataset. The accuracy of the present model is compared with that of the earlier theoretical models. Finally, an explicit correlation for predicting the flow non-uniformity of MMC heat sinks is proposed.

2. One-dimensional thermal-hydraulic modeling of MMC heat sinks

2.1. Problem formulation

The problem considered in this paper concerns the single-phase forced convective flow within an MMC heat sink with plate-fins. The MMC heat sink comprises two parts: a fluid-distributing manifold and a substrate with microchannels, which are shown in Fig. 1(a). The bottom of the substrate is subjected to a uniform heat flux condition. The two manifold inlets are located on the opposite sides of the heat sink. The main fluid streams enter these two manifold inlets and flow along the y (or $-y$) direction, distributing the fluid into the microchannels, as shown in Fig. 1(b). The fluid undergoes a complex flow path including three 90-degree turns. The flow initially makes a 90-degree turn from the y (or $-y$) direction to the $-z$ direction to enter the top of the microchannels. After impinging on the base of the microchannels, it takes another 90-degree turn from the $-z$ direction to the x (or $-x$) direction. The liquid takes heat away and finally exits through a manifold outlet by making a 90-degree turn from the x (or $-x$) direction to the z direction. The following assumptions are made in analyzing the problem:

1. Steady-state, laminar, and incompressible flow with negligible gravitational effects and viscous dissipation is considered.
2. Heat transfer through the fluid-solid interface occurs at the fin and the primary surfaces of the microchannels, while heat transfer

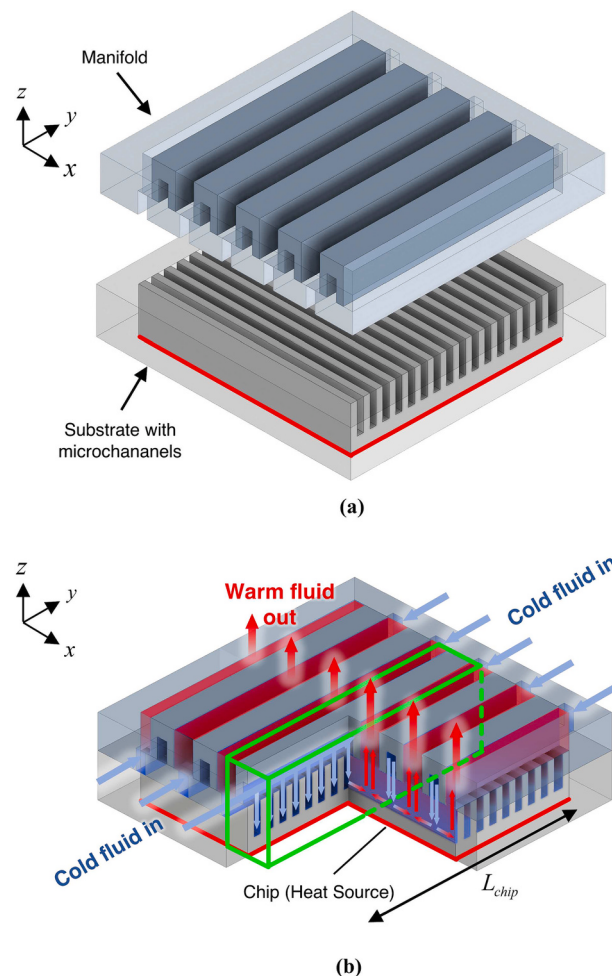


Fig. 1. Schematic of MMC heat sink. (a) Exploded view of MMC heat sink. (b) Three-quarter view of MMC heat sink. The region encapsulated by the green lines indicates the fluid and solid regions of a single manifold channel and underlying microchannels. (For interpretation of the references to colour in this figure legend, the reader is referred to the web version of this article.)

through the manifold wall is neglected.

Justification of the assumption: The previous study suggests that heat transfer at the manifold-fluid interface is negligible. Wei et al. [36] demonstrated in their 3-D numerical simulation that neglecting heat transfer through the manifold wall resulted in only a 2.5% variation in the average chip temperature compared to when heat transfer through the manifold wall is included.

3. The hydrodynamically and thermally developing flow is assumed for fluid flow within the microchannels, while the hydrodynamically fully-developed flow is assumed for the main fluid stream within the manifold.

Justification of the assumption: The hydrodynamic and thermal flow conditions in MMC heat sinks have been investigated in the previous studies. The results from the previous studies justify that the fully-developed flow assumption at the manifold inlet is valid to accurately predict the thermal performance of MMC heat sinks. Tang et al. [28] and Arie et al. [39] reported that numerical models with the fully-developed flow condition at the manifold inlet successfully predicts the thermal performance of MMC heat sinks to within the errors of 7% and 11%, respectively. On the other hand, the prior studies have highlighted that

the flow passing through the microchannels is in the hydrodynamically and thermally developing flow regime due to its short dimensionless hydraulic and thermal flow lengths. Jung [15] showed that the friction factor within the microchannels exceeds the predicted value for the fully-developed flow due to hydrodynamically developing effects. Keramani et al. [17] reported that the Nusselt number within the microchannels increases with the increase in the channel Reynolds number, indicating thermally developing flow within the microchannels.

The region encapsulated by the green lines in Fig. 1(b) represents fluid and solid regions of a single manifold channel and underlying microchannels. In order to analyze heat transfer and fluid flow within the MMC heat sink, it is necessary to solve the conjugate heat transfer problem which comprises a set of governing partial differential equations over the fluid and solid regions. The governing equations in the

differential form are as follows:

Continuity equation:

$$\nabla \cdot \mathbf{u} = 0 \quad (1)$$

Momentum equations:

$$\rho(\mathbf{u} \cdot \nabla)\mathbf{u} = -\nabla p + \nabla \cdot \boldsymbol{\tau} \quad (2)$$

Energy equation for the fluid region:

$$\rho c_p (\mathbf{u} \cdot \nabla) T = \nabla \cdot (k_f \nabla T) \quad (3)$$

Energy equation for the solid region:

$$\nabla \cdot (k_s \nabla T) = 0 \quad (4)$$

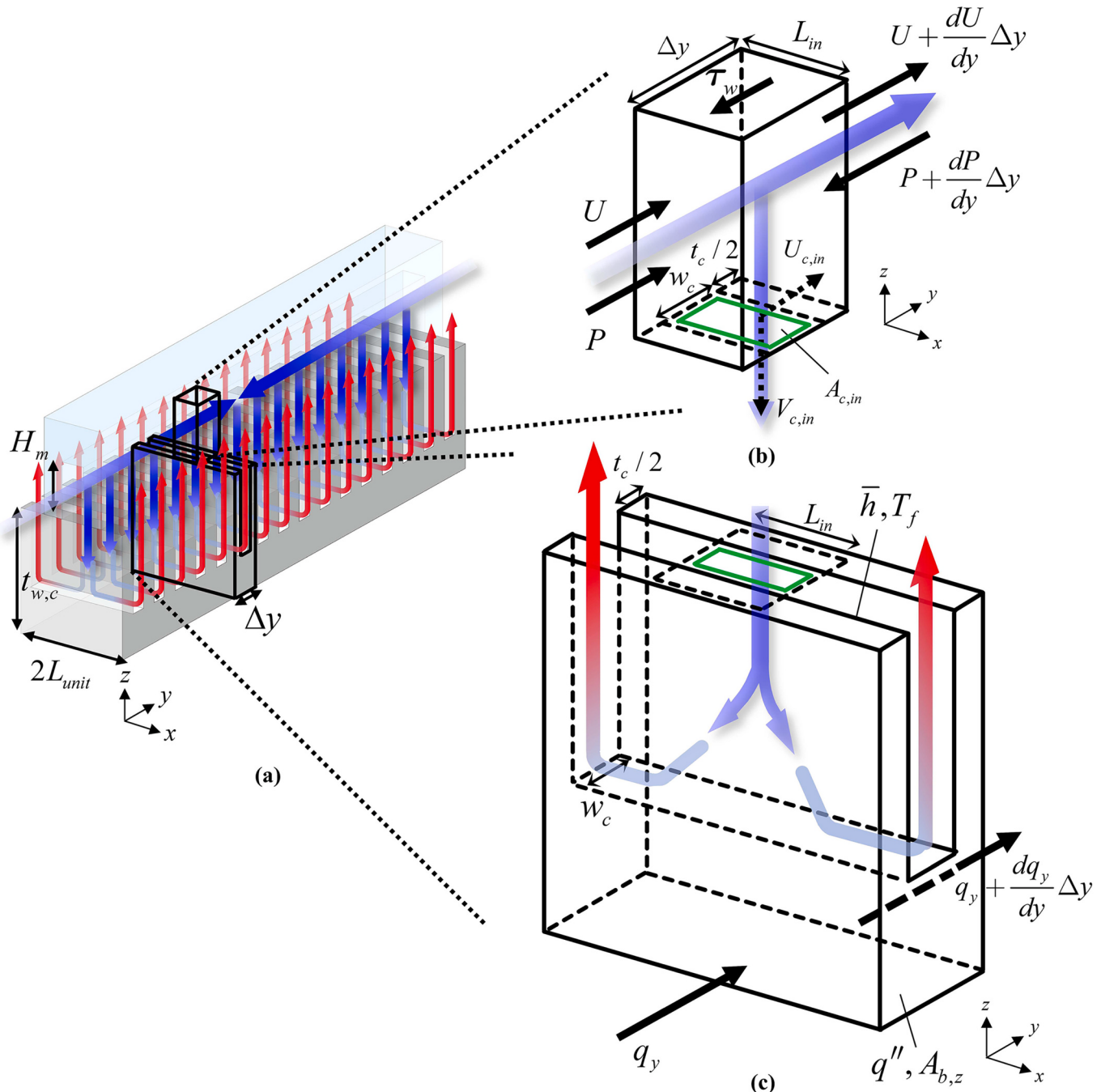


Fig. 2. Control volume definitions to derive one-dimensional governing equations. (a) Schematic of single manifold channel and underlying microchannels. (b) 3-D schematic of the control volume for the fluid region within the manifold conduit. (c) 3-D schematic of the control volume for the solid region within the substrate with microchannels.

where \mathbf{u} , p , τ , T indicate the velocity vector, the static pressure, the shear stress tensor, and the temperature, respectively.

2.2. Derivation of one-dimensional governing equations

To transform the governing partial differential equations into the ordinary differential equations that could be solved analytically, the integral analysis is performed over appropriately-defined two separate control volumes in the fluid and solid regions within the MMC heat sink, shown in Fig. 2(a). Specifically, the control volume in the fluid region, depicted in Fig. 2(b), includes the dividing flow junction where the main fluid stream branches off from the manifold to the microchannels; the control volume in the solid region, depicted in Fig. 2(c), incorporates an individual microchannel and its substrate. These appropriately-defined two separate control volumes in the fluid and solid regions enable the transformation of the governing equations in the form of three-dimensional partial differential equations into one-dimensional ordinary differential equations. If the control volumes are defined arbitrarily, the governing equations are in the form of three-dimensional partial differential equations, which could not be solved analytically. Based on the integral analysis over the control volumes defined above, the governing equations in integral form are established.

2.2.1. One-dimensional momentum equation

The continuity and momentum equations in integral form over the fluid control volume depicted in Fig. 2(b) are given as

$$\int_{CS} \mathbf{u} \cdot \mathbf{n} dA = 0 \quad (5)$$

$$\int_{CS} \rho(\mathbf{u} \cdot \mathbf{n})\mathbf{u} dA = - \int_{CS} p\mathbf{n} dA + \int_{CS} \tau \cdot \mathbf{n} dA \quad (6)$$

where \mathbf{n} indicates the surface normal vector. The integral form of the continuity equation, Eq. (5), yields

$$V_{c,in} = - \frac{A_{m,in}}{A_{c,in}} \left(\frac{dU}{dy} \Delta y \right) \quad (7)$$

where $A_{m,in}$ and $A_{c,in}$ are the cross-sectional areas of the manifold inlet and the microchannel inlet, respectively; U is the average velocity of the main fluid stream in the y direction, which is defined by the volume flow rate of the main fluid stream divided by $A_{m,in}$, and $V_{c,in}$ is the average velocity of the branching flow in the $-z$ direction, which is defined by the volume flow rate of the branching flow divided by $A_{c,in}$; Δy is the microchannel spacing which is equal to $w_c + t_c$.

The momentum equations in integral form, shown in Eq. (6), represent the balances of momentum in the x , y , and z directions over the control volume. In the x direction, the momentum balance reduces to zero due to the absence of momentum flow. In the z direction, the rate of change of the momentum associated with the branching flow is balanced by the net force, but this net force exerted to the fluid is not of interest in this study for analyzing fluid flow within the manifold. Therefore, in the derivation of one-dimensional momentum equation, the momentum balance in the y direction only is considered. The momentum balance across the control volume surfaces in the y direction can be expressed as follows:

$$\frac{dP}{dy} = - \tau_w \left(\frac{L_{p,m,in}}{A_{m,in}} \right) - 2\rho U \frac{dU}{dy} - \rho U_{c,in} V_{c,in} \left(\frac{A_{c,in}}{A_{m,in} \Delta y} \right) \quad (8)$$

where P , τ_w , $L_{p,m,in}$, and $U_{c,in}$ are the average static pressure at the control volume surface perpendicular to the y direction, the average wall shear stress acting on the control volume surfaces, the perimeter of the manifold inlet, and the average velocity of the branching flow in the y direction at the microchannel inlet, respectively. The average velocity of the branching flow in the y direction at the microchannel inlet can be

expressed as

$$U_{c,in} = \gamma U \quad (9)$$

where γ is the static pressure regain coefficient [40–42]. In this study, γ is fixed at 1.2, based on the value suggested in the previous experimental study on the fluid-distributing manifold [40]. The average wall shear stress acting on the control volume surfaces can be estimated by using the friction factor through a duct as follows:

$$\tau_w = f_m \left(\frac{1}{2} \rho U^2 \right) \quad (10)$$

where f_m is the friction factor for the fully-developed flow within a duct, suggested by Muzychka and Yovanovich [43].

By substituting Eqs. (7, 9–10) into Eq. (8), the momentum balance in the y direction reduces to

$$\frac{dP}{dy} = - f_m \left(\frac{1}{2} \rho \frac{L_{p,m,in}}{A_{m,in}} \right) U^2 + \rho(2 - \gamma)U \left(- \frac{dU}{dy} \right) \quad (11)$$

The term on the left hand side represents the static pressure gradient along the direction of the main fluid stream within the manifold. The first term on the right hand side indicates the frictional pressure drop due to the wall shear stress, while the second term represents the static pressure recovery or static pressure rise due to the branching flow.

As the fluid which branches off from the manifold flows through the microchannel and exits via the manifold outlet, the relationship for the pressure drop for the flow between the cross-section of the fluid control volume, perpendicular to the y direction and the manifold outlet can be obtained by using the modified Bernoulli equation:

$$P - P_{m,out} = \frac{1}{2} \rho V_{m,out}^2 + \Delta P_{cf} + \Delta P_{minor} + \Delta P_{m,out} \quad (12)$$

where $P_{m,out}$, ΔP_{cf} , ΔP_{minor} , $\Delta P_{m,out}$, and $V_{m,out}$ are the static pressure at the manifold outlet, the frictional pressure drop across the microchannel, the minor pressure losses arising from three 90-degree bends in the fluid path, as well as a contraction and an expansion of the flow as it enters and exits the microchannels, the pressure drop across the manifold outlet conduit, and the average velocity of the flow at the manifold outlet, respectively.

The definition of each pressure drop term is described in Table 1, and the friction factors and the minor loss coefficient required to calculate these pressure drops are summarized in Table 2. The fluid average velocity at the manifold outlet, $V_{m,out}$, is obtained in terms of U from the integral form of the continuity equation over the fluid control volume:

$$V_{m,out} = \left(\frac{A_{m,in}}{A_{m,out}} \right) \left(\frac{L_{chip}}{2n} \right) \frac{dU}{dy} \quad (13)$$

where n and L_{chip} indicate the number of the microchannels and the length of the chip, respectively. By substituting each pressured drop term and the fluid average velocity at the manifold outlet into Eq. (12), the following form of the equation is obtained:

$$P - P_{m,out} = \frac{1}{2} \rho (\zeta + K_{minor}) \left(\frac{dU}{dy} \right)^2 \quad (14)$$

Table 1
Definitions of pressure drops.

Pressure drops	Definitions
Frictional pressure drop across the microchannels (ΔP_{cf})	$f_c \left(\frac{1}{2} \rho V_c^2 \right) \frac{L_{p,c} L_{flow}}{A_c}$
Minor pressure losses (ΔP_{minor})	$K_{minor} \left(\frac{1}{2} \rho V_c^2 \right)$
Frictional pressure drop across the manifold outlet conduit ($\Delta P_{m,out}$)	$f_{m,out} \left(\frac{1}{2} \rho V_{m,out}^2 \right) \frac{L_{p,m,out} L_{m,out}}{A_{m,out}}$

* Fluid average velocity within the microchannels.

Table 2

Correlations for friction factors and minor loss coefficients.

Coefficients	Correlations
Poiseuille number for the manifold (Muzychka and Yovanovich [43])	$f_m Re_m = \frac{12}{\sqrt{\epsilon}(1+\epsilon)\left[1 - \frac{192}{\pi^5} \tanh\left(\frac{\pi}{2\epsilon}\right)\right]}$
Poiseuille number for the microchannel (Muzychka and Yovanovich [43])	$f_c Re_c = \left[\left(\frac{3.44}{\sqrt{x^*}}\right)^2 + \left(\frac{12}{\sqrt{\epsilon}(1+\epsilon)\left[1 - \frac{192\epsilon}{\pi^5} \tanh\left(\frac{\pi}{2\epsilon}\right)\right]}\right)^2\right]^{1/2}$
Poiseuille number for the manifold outlet conduit (Muzychka and Yovanovich [43])	$f_{m,out} Re_{m,out} = 24$
Minor loss coefficient	$K_{minor} = (K_{90,out} + K_e) \left(\frac{V_{c,in}}{V_c}\right)^2 + (K_{90,in} + K_c)$
90-deg bend loss coefficient at the microchanenl inlet (Duan and Muzychka [44], Kondo and Matsushima [45])	$K_{90,in} = \begin{cases} 3.64 - 9.15\left(\frac{H_c}{L_{in}}\right) + 10.67\left(\frac{H_c}{L_{in}}\right)^2 - 4.29\left(\frac{H_c}{L_{in}}\right)^3 \\ (0 < H_c/L_{in} \leq 1.4) \\ 0.5\left(\frac{1+L_{in}/2H_c}{2}\right)^2 (H_c/L_{in} > 1.4) \end{cases}$
90-deg bend loss coefficient at the microchannel outlet (Duan and Muzychka [44], Kondo and Matsushima [45])	$K_{90,out} = \begin{cases} 3.64 - 9.15\left(\frac{L_{out}}{4H_c}\right) + 10.67\left(\frac{L_{out}}{4H_c}\right)^2 - 4.29\left(\frac{L_{out}}{4H_c}\right)^3 \\ (0 < L_{out}/4H_c \leq 1.4) \\ 0.5\left(\frac{1+2H_c/L_{out}}{2}\right)^2 (L_{out}/4H_c > 1.4) \end{cases}$
Contraction loss coefficient (Kays and Crawford [46])	$K_c = 0.4(1 - \sigma^2) + 0.4$
Expansion loss coefficient (Kays and Crawford [46])	$K_e = (1 - \sigma)^2 - 0.4\sigma$

In Eq. (14), ζ is the combination of the friction factors and the geometric parameters, which is defined as

$$\zeta = \left(\frac{A_{m,in}L_{chip}}{2n}\right)^2 \left[f_c \left(\frac{L_{p,c}L_{flow}}{A_c}\right) \left(\frac{1}{2A_c}\right)^2 + \left(1 + f_{m,out} \frac{L_{p,m,out}t_{w,m}}{A_{m,out}}\right) \left(\frac{1}{A_{m,out}}\right)^2\right] \quad (15)$$

By differentiating Eq. (14) with respect to y and substituting it into Eq. (11) with zero gauge pressure at the outlet, the one-dimensional momentum equation is finally derived in the form of a second-order non-linear ordinary differential equation as

$$\left(\frac{dU}{dy}\right) \left(\frac{d^2U}{dy^2}\right) + \left(\frac{2-\gamma}{\zeta + K_{minor}}\right) U \frac{dU}{dy} + \left[\frac{f_m}{2(\zeta + K_{minor})} \frac{L_{p,m,in}}{A_{m,in}}\right] U^2 = 0 \quad (16)$$

The appropriate boundary conditions are $U(0) = U_{in}$ and $U(L_{chip}/2) = 0$.

2.2.2. One-dimensional energy equation

The integral form of the energy equation over the solid control volume, shown in Fig. 2(c), is given in Eq. (17).

$$\int_{CS} (k_s \nabla T) \cdot \mathbf{n} dA = 0 \quad (17)$$

The energy balance across the control volume surfaces is represented by considering conduction heat transfer within the y di-

rection and appropriate boundary conditions; the bottom surface of the substrate is uniformly heated by a heat dissipating chip, and the fluid takes heat away from the chip at the fluid-solid interface by convection. The overall energy balance across the control volume surfaces is expressed as follows:

$$\frac{dq_y}{dy} \Delta y + \eta_o \bar{h} A_{tot} (T_b - T_f) = q'' A_{b,z} \quad (18)$$

where q_y , q'' , η_o , \bar{h} , A_{tot} , $A_{b,z}$, T_b , and T_f are the conduction heat transfer rate in the y direction, the heat flux dissipated by the chip, the overall fin efficiency, the average heat transfer coefficient, the total wetted surface area, the cross-sectional area of the control volume surface perpendicular to the z direction, the base temperature, and the bulk mean fluid temperature, respectively. Since

$$q_y = -k_s A_{b,y} \frac{dT}{dy} \quad (19)$$

where $A_{b,y}$ and \bar{T} are, respectively, the cross-sectional area of the control volume surface perpendicular to the y direction and the temperature at the control volume center, Eq. (18) reduces to

$$\frac{d^2 \bar{T}}{dy^2} - \eta_o \bar{h} \frac{A_{tot}}{k_s A_{b,y} \Delta y} (T_b - T_f) = -q'' \frac{A_{b,z}}{k_s A_{b,y} \Delta y} \quad (20)$$

Utilizing geometric parameters $\alpha = (w_c + t_c + 2H_c)/(w_c + t_c)$ and $\Delta y = w_c + t_c$ reduces the above equation to

$$\frac{d^2 \bar{T}}{dy^2} - \frac{\eta_o}{k_s t_b} \alpha \bar{h} (T_b - T_f) = -\frac{q''}{k_s t_b} \quad (21)$$

where t_b is the thickness of the substrate. Eq. (21) is the energy equation in the form of second-order linear ordinary differential equation. The boundary conditions related to the energy equation are $\left.\frac{d\bar{T}}{dy}\right|_{y=0} = 0$ and

$$\left.\frac{d\bar{T}}{dy}\right|_{y=L_{chip}/2} = 0.$$

The unknown average heat transfer coefficient, \bar{h} , can be estimated by the correlation of the Nusselt number for simultaneously developing flow suggested by Muzychka and Yovanovich [43], which is

$$\bar{Nu} = \frac{\bar{h} D_c}{k_f} = \frac{1.772}{\left[1 + (1.909 Pr^{1/6})^{9/2}\right]^{2/9}} \frac{1}{\sqrt{x^*}} \quad (22)$$

where D_c , k_f , and Pr are the hydraulic diameter of the cross-section of the microchannels, the thermal conductivity of the fluid, and the Prandtl number of the fluid, respectively; x^* is the dimensionless thermal flow length which is defined as

$$x^* = \frac{L_{flow}}{Re_c Pr D_c} \quad (23)$$

where Re_c is the Reynolds number of the flow within the microchannels.

The base tempeerature can be estimated from the temperature at the control volume center based on the assumption of a linear temperature variation within the substrate.

$$T_b = \bar{T} - q'' \left(\frac{t_b/2}{k_s}\right) \quad (24)$$

The bulk mean fluid temperature is defined by the average of the inlet and outlet temperatures.

$$T_f = \frac{T_{in} + T_{out}}{2} \quad (25)$$

where

Table 3

Thermophysical properties of materials used in the one-dimensional model and 3-D numerical simulation.*

Material properties	DI water [47]	Silicon [48]
ρ [kg/m ³]	$1.025 \times 10^{-5}T^3 - 1.330 \times 10^{-2}T^2 + 4.935T + 436.4$	2330
c_p [J/kg·K]	$-2.879 \times 10^{-5}T^3 + 3.778 \times 10^{-2}T^2 - 15.14T + 6101$	$2.966 \times 10^{-6}T^3 - 5.091 \times 10^{-3}T^2 + 3.183T + 140.3$
k [W/m·K]	$2.228 \times 10^{-8}T^3 - 3.059 \times 10^{-5}T^2 + 1.391 \times 10^{-2}T - 1.414$	$-7.342 \times 10^{-6}T^3 + 9.854 \times 10^{-3}T^2 - 4.652T + 859.9$
μ [kg/m·s]	$-1.248 \times 10^{-9}T^3 + 1.353 \times 10^{-6}T^2 - 4.932 \times 10^{-4}T + 6.071 \times 10^{-2}$	-

* FTemperature, T in Kelvin.

$$T_{out} = T_{in} + \frac{q'' A_{b,z}}{\dot{m}_c c_p} \quad (26)$$

Thermophysical properties of materials in the one-dimensional momentum and energy equations are temperature dependent, and these temperature-dependent thermophysical properties of materials are provided in **Table 3**. Note that reference temperatures to estimate the thermophysical properties of the materials are different for each fluid and solid region. Specifically, the reference temperatures for the fluid properties within the manifold and the microchannels are the fluid inlet temperature (T_{in}) and the bulk mean fluid temperature (T_f), respectively. The reference temperature for the solid properties is the temperature at the center of the solid control volume (\bar{T}).

Finally, the set of momentum and energy equations in the form of ordinary differential equations, Eqs. (16) and (21), is solved simultaneously. By solving these ordinary differential equations, the flow distribution among the microchannels and the resultant non-uniform temperature distribution within the substrate are obtained. Specifically, the momentum and energy equations are first transformed into the set of algebraic equations using the finite difference method. The detailed derivation procedure to obtain these finite difference equations from the one-dimensional momentum and energy equations is illustrated in

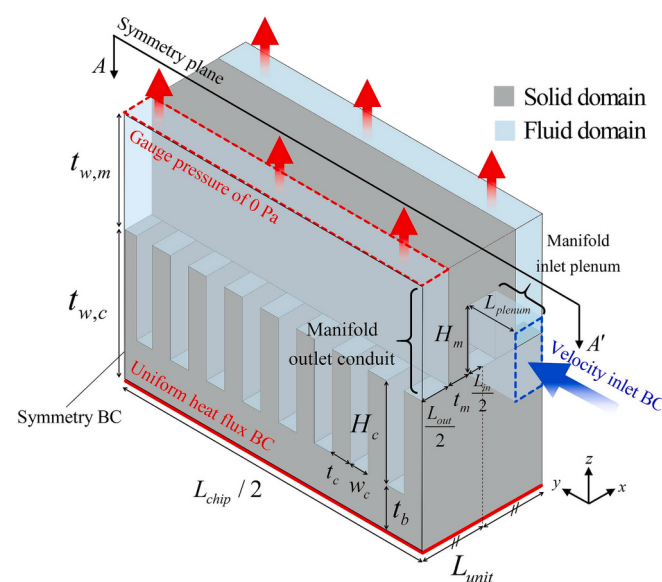


Fig. 3. The computational domain of MMC heat sinks. The computational domain consists of the fluid regions within the single manifold and the underlying microchannels and the solid region of the substrate with its microchannels.

Table 4

The grid independence test result.

Grid	# of elements	$T_{b,\text{avg}}$ [°C]	$\left \frac{T_{b,\text{avg}}^{i+1} - T_{b,\text{avg}}^i}{T_{b,\text{avg}}^i} \right [\%]$	ΔP [Pa]	$\left \frac{\Delta P^i - \Delta P^{i+1}}{\Delta P^i} \right [\%]$
Grid 1	3,302,835	37.97	-	3577.31	-
Grid 2	9,184,911	37.85	0.296	3676.67	2.70
Grid 3	14,360,703	37.92	0.16	3969.90	0.55

Note: The grid independence test is conducted for the MMC heat sink with the geometry of M(500–440–220–250)W30H150T30.

Appendix A. The obtained set of algebraic equations is simultaneously solved by *fsove* solver in MATLAB® with Levenberg-Marquardt algorithm, and the calculation is completed within a few seconds per each case.

3. 3-D numerical simulation

3.1. Computational domain and boundary conditions

The 3-D numerical simulation aims to verify the accuracy of the one-dimensional model in predicting the flow non-uniformity among the microchannels and the resultant temperature distribution within the substrate. The computational domain of the 3-D numerical simulation is depicted in **Fig. 3**. It consists of the fluid domain within a single manifold and the underlying microchannels, and the solid domain of the microchannels including its substrate. Over the computational domain, the conjugate heat transfer problem is solved using the set of governing equations in Eqs. (1–4) along with the boundary conditions, described in **Section 2.1** Problem formulation section. De-ionized (DI) water, with the inlet temperature of 23°C, is used for the fluid domain, and silicon is used for the solid domain. The temperature-dependent thermophysical properties of materials used in the 3-D numerical simulation are provided in **Table 3**. The applicable ranges of material properties are from 296 K to 373 K for DI water and 300 K to 500 K for silicon. A commercial CFD package, ANSYS Fluent v21 R1 is used to conduct the numerical simulation. The mesh configuration for the numerical simulation consists of conformal polyhedral elements near the fluid-solid interfaces and hexahedral elements in the bulk regions of both the solid and fluid domains. The length of one side of the element is approximately 2 μm so that it can fully resolve the flow and heat transfer characteristics within the boundary layers.

3.2. Grid independence test

A grid independence test is performed to ensure that the results of the 3-D numerical simulation are invariant to the grid resolution. An MMC heat sink with the channel aspect ratio (AR) of 5 and with the unit cell length (L_{unit}) of 500 μm is chosen for the grid independence test. The

Table 5

The range of geometric parameters for the parametric study.

L_{unit} [μm]	L_{in} [μm]	L_{out} [μm]	t_m [μm]	w_c [μm]	H_c [μm]	t_c [μm]
500	400	200	200	20–50	150–300	20–50
830	664	332	332	20–50	150–300	20–50
1000	800	400	400	20–50	150–300	20–50

Table 6

The range of key dimensionless parameters.

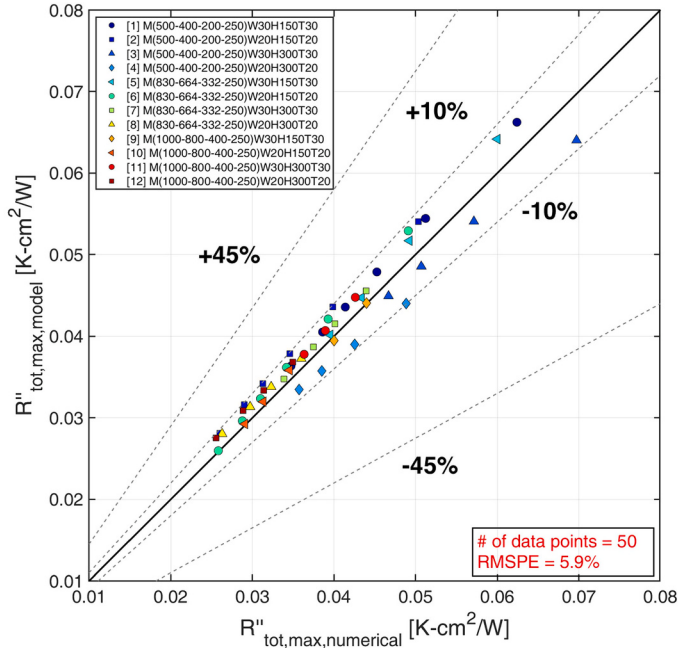
$Re_{m,in}$	$AR (= H_c/w_c)$	x^+	x^*
560–3190	3–15	0.012–0.123	0.002–0.023

Table 7

Dimensions of the fixed geometries for each structure in the parametric study.

Structures	Geometry	Dimensions
Manifold	L_{plenum}	400 μm
	H_m	250 μm
Substrate with microchannels	$t_{w,m}$	500 μm
	L_{chip}	5 mm
	$t_{w,c}$	500 μm

average base temperature and the pressure drop are obtained from the 3-D numerical simulation for the total flow rate of 400 mL/min and the heat flux of 400 W/cm². Successive grid refinements are carried out, and Table 4 shows that the differences in the average base temperature and the pressure drop between Grid 2 (9.2 M elements) and Grid 3 (14.4 M elements) are less than 1%. Therefore, the mesh generation setting from Grid 2 is selected as the standard for the parametric study. The computational time of Grid 2 required for the convergence is



Previous models with uniform flow distribution assumption

(a)

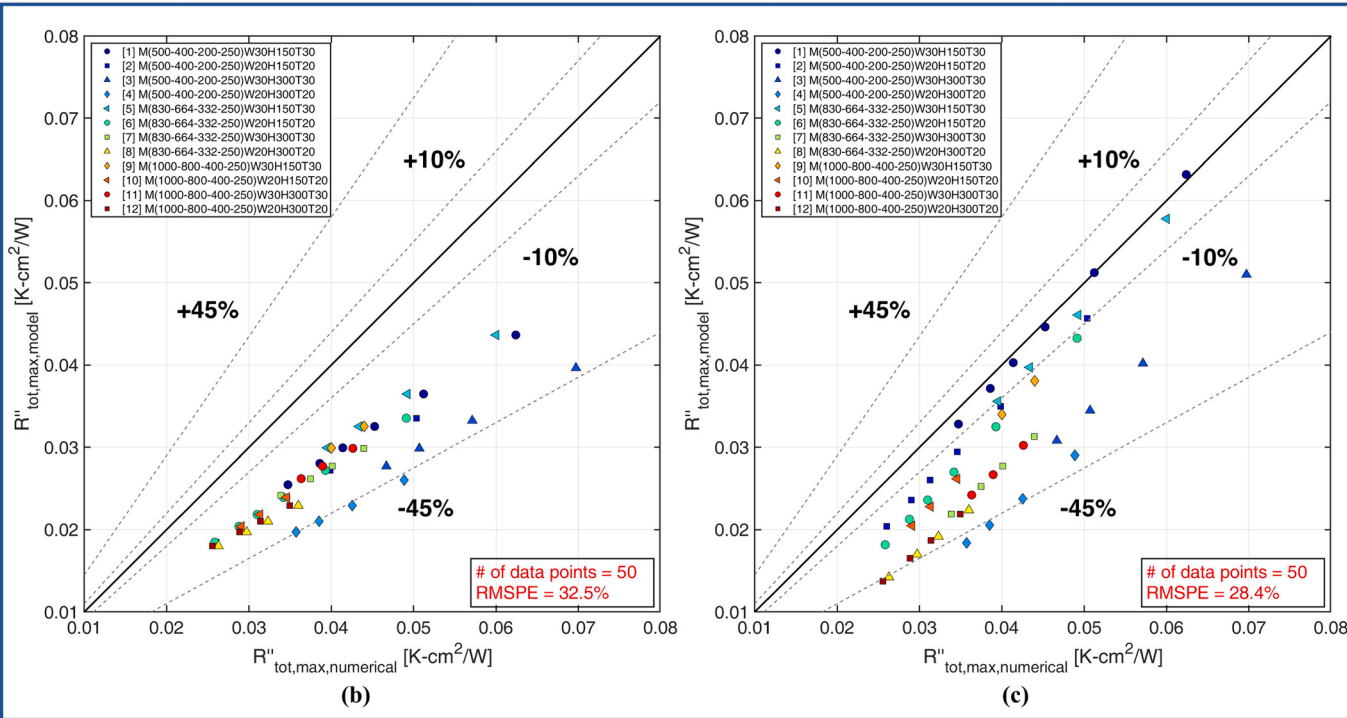


Fig. 4. The prediction results of the total thermal resistance of MMC heat sinks with various manifold and microchannel geometries based on the models. (a) The prediction result using the one-dimensional model. The present model predicts the total thermal resistance of MMC heat sinks within the RMSPE of 6%. (b) The prediction result using the uniform flow distribution model suggested by Copeland et al. [13]. The suggested model underpredicts the total thermal resistance of MMC heat sinks up to the error of 47%. (c) The prediction result using the uniform flow distribution model proposed by Yuruker et al. [51]. The proposed model still underestimates the total thermal resistance of MMC heat sinks, with a maximum error of 49%. Here, each MMC heat sink is identified using the nomenclature $M(L_{unit}L_{in}L_{out}H_m)W(w_c)H(H_c)T(t_c)$ which includes the geometric parameters of both the manifold and the microchannels.

approximately 20 h using Intel Core i9 24-core 3.0 GHz processors.

3.3. Range of the parametric study

An extensive parametric study on various geometric parameters of an MMC heat sink is performed using 3-D numerical simulation for the validation of the proposed one-dimensional model. Before conducting the parametric study, a new nomenclature is suggested to easily identify the individual MMC heat sinks. The nomenclature, $M(L_{unit} \cdot L_{in} \cdot L_{out} \cdot H_m)W(w_c)H(H_c)T(t_c)$, includes the geometric parameters of both the manifold and the microchannels, and it will be used in the [Results and discussion](#) section. Since the MMC heat sink involves various geometric parameters, dominant geometric parameters that primarily affect the thermal-hydraulic performance of the MMC heat sinks are determined based on a sensitivity analysis from the previous literature [37,49,50]. In this study, a total of 15 distinct geometries for the MMC heat sinks are investigated, encompassing three manifold configurations and five microchannel designs. Each of the three manifold configurations is characterized by its unit cell length, with L_{unit} values of 500, 830, and 1000 μm . These correspond to the number of manifold, N_m , of 5, 3, and 2.5, respectively, for a chip size of $5 \times 5 \text{ mm}^2$. Each of the five microchannel designs features a channel aspect ratio (AR) ranging from 3 to 15, with channel heights of either 150 or 300 μm . On the other hand, the height of the manifold, H_m , and the ratio of the manifold inlet width to the manifold outlet width, (L_{in}/L_{out}), are fixed to 250 μm and 2, respectively. Additionally, the microchannel wall thickness is assumed to be the same with the width of the microchannel. The detailed information regarding the ranges of dimensions for varying geometric parameters is summarized in [Table 5](#). The other geometric parameters fixed in the parametric study are described in [Table 7](#). For the operating conditions, the total flow rate varies from 100 to 400 mL/min, and the uniform heat flux of 400 W/cm² is applied at the bottom of the substrate. The ranges of the dimensionless parameters are outlined in [Table 6](#).

4. Results and discussion

4.1. Prediction of the thermal performance and flow non-uniformity of MMC heat sinks

The thermal performance of an MMC heat sink is defined by the total thermal resistance based on the maximum base temperature:

$$R_{tot,max}'' = \frac{T_{b,max} - T_{in}}{q} \quad (27)$$

where $T_{b,max}$ is the maximum base temperature of the microchannels. [Fig. 4](#) shows the predictions of the total thermal resistance of the MMC heat sinks based on the one-dimensional model and the previous models suggested by Copeland et al. [13] and Yuruker et al. [51], both of which are based on the assumption of uniform flow distribution. The prediction using the one-dimensional model shows good agreement with the total thermal resistance of the MMC heat sinks estimated by 3-D numerical simulation to within the root mean square percentage error (RMSPE) of 6%. In contrast, the previous models underestimate the total thermal resistance by up to 49%, since they do not take into account the non-uniform flow distribution among the microchannels and the resultant non-uniform temperature distribution within the substrate. By accounting for the flow non-uniformity among the microchannels for the first time, the proposed one-dimensional model shows a significant error reduction of 82% compared to the models based on the assumption of uniform flow distribution.

The flow non-uniformity of an MMC heat sink is defined by the interquartile-based coefficient of variation (CV):

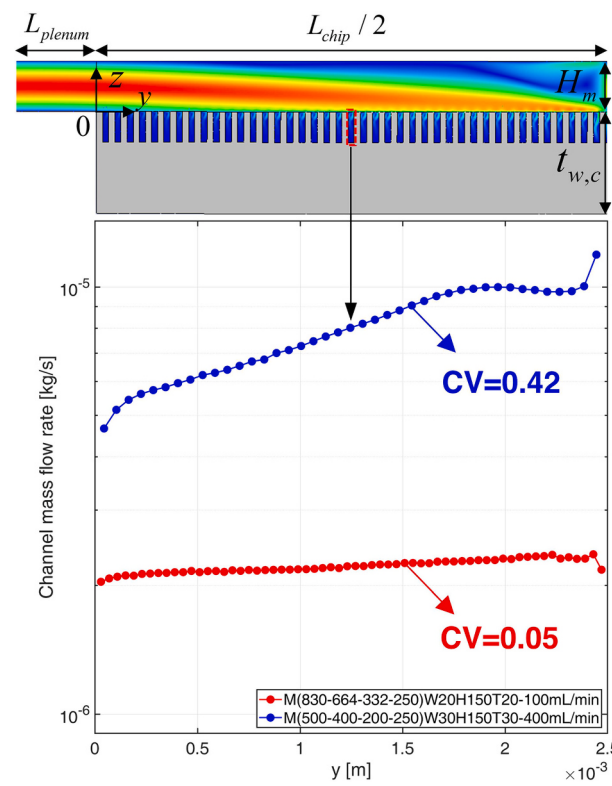


Fig. 5. The non-uniform flow distributions among the microchannels depending on the CV. The flow distribution becomes uneven as the CV increases. The schematic above the graph represents the y-z cross-section of the computational domain, which corresponds to the A-A' section in [Fig. 3](#), in the 3-D numerical simulation. The colored fluid region indicates the magnitude of the fluid velocity.

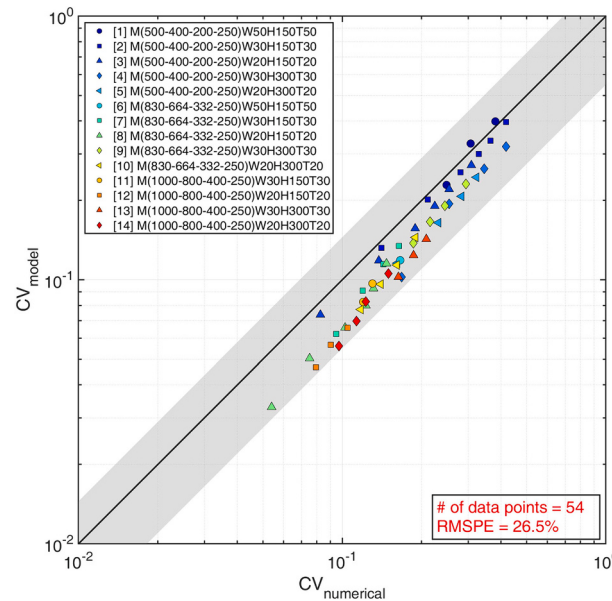


Fig. 6. The prediction result of the flow non-uniformity (CV) of MMC heat sinks with various manifold and microchannel geometries. The present model predicts the CV within the RMSPE of 26%. The grey region indicates the range of error up to $\pm 45\%$.

$$CV = \frac{IQR}{\text{med}(\dot{m}_c)} \quad (28)$$

where IQR and $\text{med}(\dot{m}_c)$ indicate the interquartile range and median of the flow distribution, respectively. The interquartile range of the flow distribution is defined by the difference between 75-th and 25-th percentiles of the channel flow rates. The interquartile-based CV is widely used in statistical analysis as a measure of the unevenness of a given dataset, owing to its low sensitivity to outliers which can lead to misinterpretations of the dataset [52].

Fig. 5 illustrates the relation between the CV and the flow non-uniformity among the microchannels. As the CV increases, the flow distribution becomes uneven. The prediction result of the flow non-uniformity of MMC heat sinks using the one-dimensional model is shown in Fig. 6. The result shows that the one-dimensional model predicts the flow non-uniformity of MMC heat sinks estimated by 3-D numerical simulation within the RSMPE of 26%. On the contrary, the previous model cannot predict the flow non-uniformity since it has assumed the uniform flow distribution among the channels. Thus, the CV value estimated by the previous model turns out to be always zero, which cannot account for the flow characteristics of the MMC heat sinks.

In order to measure the extent of a temperature variation within the substrate caused by the flow non-uniformity, the temperature non-uniformity (σ_T) of an MMC heat sink is defined as follows:

$$\sigma_T = \frac{T_{b,\max} - T_{b,\text{avg}}}{T_{b,\text{avg}} - T_{in}} \quad (29)$$

where $T_{b,\text{avg}}$ is the average base temperature of the microchannels. The defined temperature non-uniformity indicates the relative difference between the maximum and average base temperatures of the microchannels. The prediction result of the temperature non-uniformity is shown in Fig. 7. The results indicate that σ_T is directly proportional to the CV. A least square fitting of the numerical dataset reveals an explicit correlation between them, which is

$$\sigma_T = 0.5CV \quad (30)$$

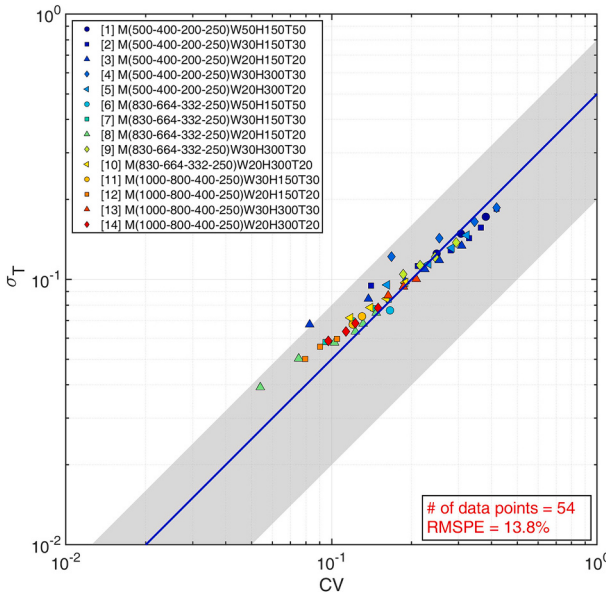


Fig. 7. The prediction result of the temperature non-uniformity(σ_T). The blue line indicates $\sigma_T = 0.5CV$, and the grey region indicates the range of error up to $\pm 60\%$. (For interpretation of the references to colour in this figure legend, the reader is referred to the web version of this article.)

4.2. Correlation for predicting the flow non-uniformity

When the main fluid stream uniformly branches off from the manifold to each microchannel, the static pressure within the manifold remains constant since the pressure drop across each of the microchannels is identical. Thus, to achieve the uniform flow distribution among the microchannels, the static pressure variation along the main fluid stream should be negligible. This corresponds to the case where the static pressure variation within the manifold is relatively small compared to the pressure drop across the microchannels:

$$\frac{\Delta P}{\Delta P_c} \ll 1 \quad (31)$$

where ΔP indicates the static pressure variation within the manifold, and ΔP_c indicates the pressure drop across the microchannels. A scale analysis is conducted based on the one-dimensional momentum equation, Eq. (11), to obtain the scale of ΔP . The scale of each term in the one-dimensional momentum equation is expressed as follows:

$$\underbrace{\Delta P}_{\text{Static pressure variation}}, \underbrace{\rho U_{in}^2}_{\text{Frictional pressure drop}} \left(\frac{L_{chip}}{Re_{m,in} D_m} \right), \underbrace{\rho U_{in}^2}_{\text{Pressure recovery due to branching flow}} \quad (32)$$

which is derived based on that the average velocity of the main fluid stream in the y direction (U) and the manifold friction factor (f_m) are respectively of the same order of magnitudes as U_{in} and $1/Re_{m,in}$; the static pressure regain coefficient (γ) is 1; the characteristic length in the y direction scales as L_{chip} . Given that $L_{chip}/(Re_{m,in} D_m)$ in the frictional pressure drop term has an order of magnitude of 0.1 under the tested operating conditions of the MMC heat sinks, the static pressure recovery becomes a dominant term on the right hand side of the Eq. (32). This is of the same order of magnitude as the dynamic pressure at the manifold inlet. Hence, ΔP is of the same order of magnitude as ρU_{in}^2 . Using this result, the explicit form of the dimensionless parameter for estimating the flow non-uniformity is expressed as follows:

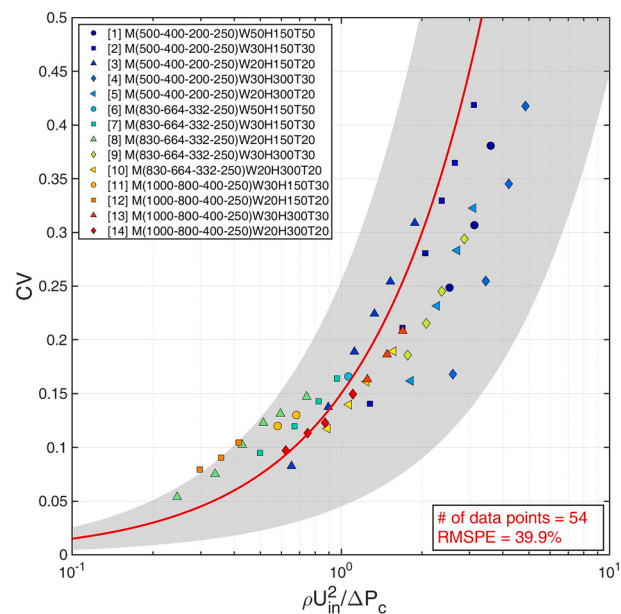


Fig. 8. The prediction result of the flow non-uniformity (CV) based on the scale analysis. The red line indicates $CV = 0.15(\rho U_{in}^2 / \Delta P_c)$. The grey region indicates the range of error up to $\pm 70\%$. (For interpretation of the references to colour in this figure legend, the reader is referred to the web version of this article.)

$$\frac{\Delta P}{\Delta P_c} \sim \frac{\rho U_{in}^2}{\Delta P_c} \quad (33)$$

where ΔP_c can be estimated by the average channel flow rate with the correlations given in [Table 2](#).

Based on the least square fitting using the numerical dataset, a proportionality constant is determined, and the following form of the explicit correlation for predicting the flow non-uniformity is suggested as a function of the proposed dimensionless parameter:

$$CV = 0.15 \left(\frac{\rho U_{in}^2}{\Delta P_c} \right) \quad (34)$$

[Fig. 8](#) shows that the prediction result of CV using the correlation in Eq. (34). The x axis is represented by the log scale. The result indicates that the proposed correlation can capture the general trend of an increase in the flow non-uniformity with an increase in the dimensionless parameter. This verifies the validity of the dimensionless parameter for predicting the flow non-uniformity of MMC heat sinks. Furthermore, the correlation suggests a useful design guideline for the MMC heat sinks: the dynamic pressure (ρU_{in}^2) at the manifold inlet should be kept smaller relative to the pressure drop across the microchannels (ΔP_c) for the uniform flow distribution among the microchannels, which is

$$\frac{\rho U_{in}^2}{\Delta P_c} < 1 \quad (35)$$

The suggested design guideline ensures that the value of CV in MMC heat sinks remains below 0.15, as indicated by Eq. (34). This result implies that the relative difference between the maximum and average base temperatures of microchannels is kept within 10%, which is shown in [Fig. 7](#). Consequently, the design of an MMC heat sink recommended by the guideline ensures the uniform temperature distribution within the substrate by promoting the uniform flow distribution among the microchannels.

5. Conclusion

Throughout this study, a one-dimensional model for predicting the thermal performance and the flow non-uniformity of manifold micro-channel (MMC) heat sinks has been proposed and validated. For this, one-dimensional governing equations are derived from integral relations of momentum and energy over appropriately-defined two separate control volumes. The derived one-dimensional governing equations are solved without introducing any fitting parameters. By solving these equations, the flow distribution among the microchannels and the resultant temperature distribution within the solid substrate are estimated. The proposed model is validated over a wide range of geometric parameters and operating conditions by using the dataset of 3-D numerical simulation. Fifty data points regarding the total thermal resistance and the coefficient of variation (CV) of the flow distribution among the microchannels have been gathered for comparison with the predictions. The applicable range of the proposed model includes the channel aspect ratio (AR) from 3 to 15, the Reynolds number ($Re_{m,in}$) at the manifold inlet from 560 to 3190, the dimensionless hydraulic flow length (x^+) from 0.012 to 0.123, and the dimensionless thermal flow length (x^*) from 0.002 to 0.023. The key findings of this study can be

highlighted as follows:

1. A one-dimensional model of an MMC heat sink which accounts for the effects of the non-uniform flow distribution on the thermal performance is developed. The present model enables the accurate prediction of the thermal performance and flow non-uniformity of an MMC heat sink: The total thermal resistance and the CV are estimated within the root mean square percentage error (RMSPE) of 6% and 26% for 50 data points, respectively. Compared to the earlier model based on the uniform flow distribution assumption, the prediction error for the thermal performance has been significantly reduced by 82%.
2. An explicit correlation for predicting the flow non-uniformity of an MMC heat sink is proposed. The correlation is derived by using a scale analysis and suggested as $CV = 0.15 \left(\frac{\rho U_{in}^2}{\Delta P_c} \right)$

The proposed correlation is validated over a range of $\rho U_{in}^2 / \Delta P_c$ from 0.25 to 4.86. The correlation shows that the flow non-uniformity becomes more severe as the magnitude of the dynamic pressure at the manifold inlet increases relative to the magnitude of the channel pressure drop. Hence, a useful design guideline for ensuring uniform flow distribution in an MMC heat sink is newly suggested: the ratio of dynamic pressure at the manifold inlet to the pressure drop across the microchannels should be kept below 1.

CRediT authorship contribution statement

Hansol Lee: Conceptualization, Investigation, Validation, Methodology, Formal analysis, Writing – original draft, Writing – review & editing. **Young Jin Lee:** Investigation, Validation, Methodology, Writing – original draft, Writing – review & editing. **Sung Jin Kim:** Supervision, Project administration, Funding acquisition, Writing – review & editing.

Declaration of competing interest

The authors declare that they have no known competing financial interests or personal relationships that could have appeared to influence the work reported in this paper.

Data availability

Data will be made available on request.

Acknowledgments

This work was supported by the National Research Foundation of Korea (NRF) grant funded by the Korea government (MSIT) (No. 2021R1A2C3011944), and by Korea Research Institute for defense Technology planning and advancement (KRIT) grant funded by the Korea government (DAPA(Defense Acquisition Program Administration)) (No. KRIT-CT-22-022). We would like to acknowledge the technical support from ANSYS Korea.

Appendix A. Derivation and detailed solving procedure for finite difference equations of the one-dimensional model

The one-dimensional momentum and energy equations are transformed into the set of algebraic equations using the finite difference method. [Fig. A.1](#) shows the pressure and velocity nodes with the staggered-grid arrangement to derive finite difference form of the one-dimensional momentum equation. The number of pressure nodes is equivalent to the number of microchannels, n , and the number of velocity nodes corresponds to $n + 1$ where $n = L_{chip}/2/\Delta y$. Using the forward difference scheme for the derivative of pressure and the central difference scheme for the derivative of velocity at the velocity node U_i gives the following finite difference form of the momentum balance, Eq. (1).

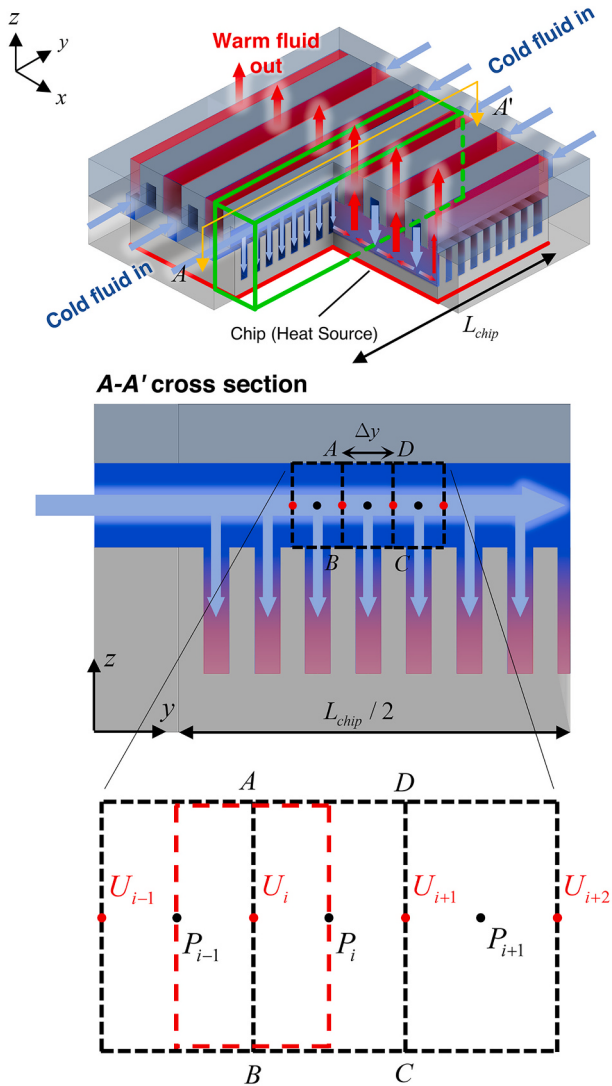


Fig. A.1. Discretization of the fluid domain within the manifold to derive the finite difference equation from the one-dimensional momentum equation.

$$P_i - P_{i-1} = -f_{m,i} \left(\frac{1}{2} \rho \frac{L_{p,m,in}}{A_{m,in}} \right) (\Delta y) U_i^2 + \rho(2-\gamma) U_i \left(\frac{U_{i-1} - U_{i+1}}{2} \right) \quad (\text{A.1})$$

The boundary conditions for the velocity nodes are $U_1 = U_{in}$ and $U_{n+1} = 0$. On the other hand, the static pressure at each pressure node can be estimated by using the modified Bernoulli equation, Eq. (12):

$$P_i - P_{m,out} = \frac{1}{2} \rho V_{m,out,i}^2 + \Delta P_{c,f,i} + \Delta P_{minor,i} + \Delta P_{m,out,i} \quad (\text{A.2})$$

The pressure drop terms on the right hand side of the equation indicate the pressure drop across the i -th microchannel. A finite difference form of each pressure drop term is simply obtained by substituting the velocities $V_{c,i}$ and $V_{m,out,i}$ into V_c and $V_{m,out}$ using the definitions in Table 1, where

$$V_{c,i} = (U_i - U_{i+1}) \frac{A_{m,in}}{2A_c} \quad (\text{A.3})$$

$$V_{m,out,i} = (U_i - U_{i+1}) \frac{A_{m,in}}{L_{out} \Delta y} \quad (\text{A.4})$$

Therefore, $2n - 1$ equations including unknown values at velocity and pressure nodes, which consist of $n - 1$ equations from the momentum balance and n equations from the modified Bernoulli equations are obtained.

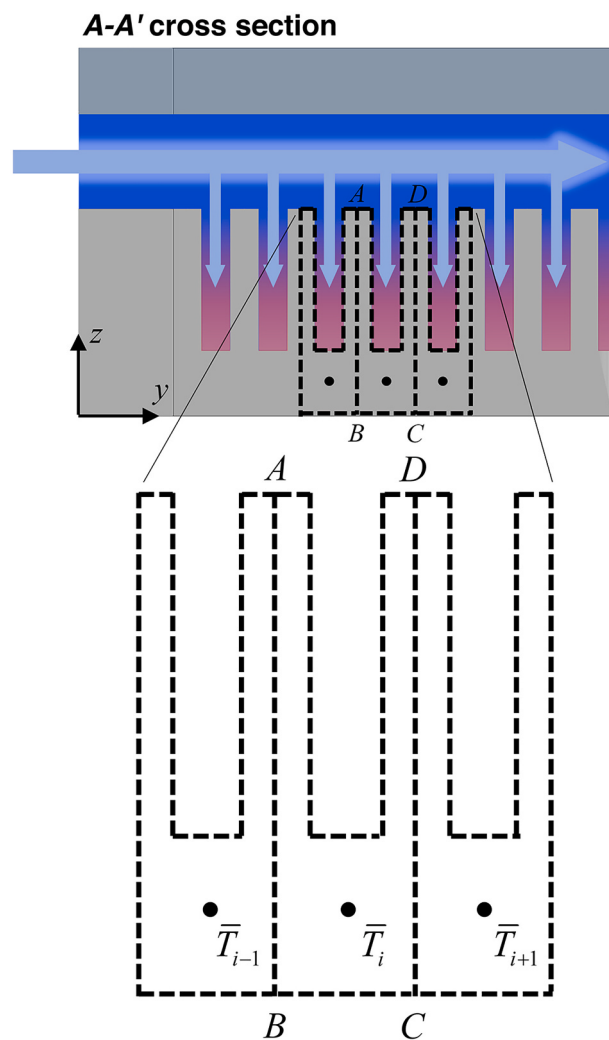


Fig. A.2. Discretization of the solid domain of the substrate with microchannels to derive the finite difference equation from the one-dimensional energy equation.

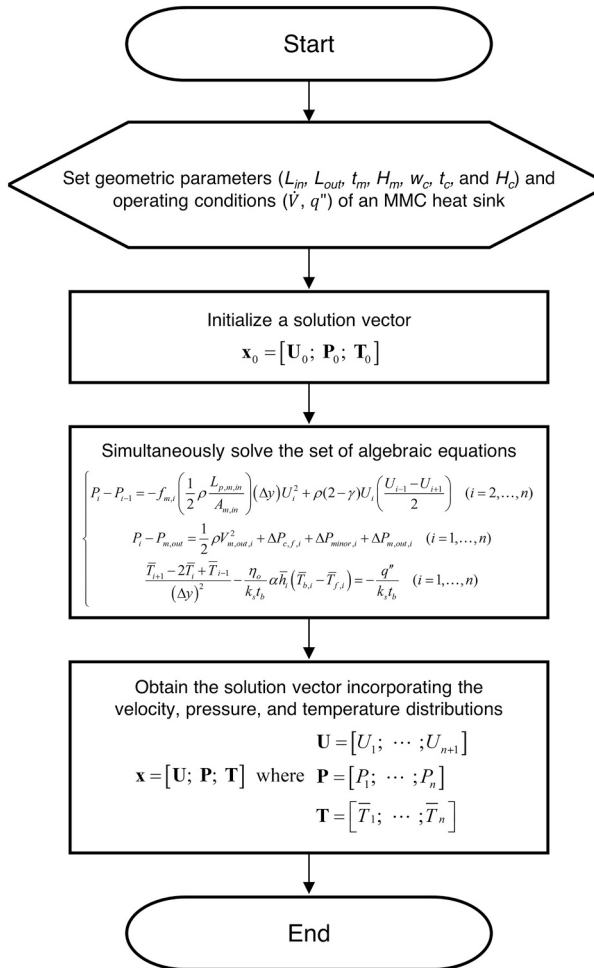


Fig. A.3. The detailed procedure for estimating the velocity, pressure, and temperature distributions of an MMC heat sink using the one-dimensional model.

Fig. A.2 shows the temperature nodes at the center of each solid control volume. The number of temperature nodes is equivalent to the number of microchannels, n . By using the central difference scheme for the derivative of temperature at the temperature node \bar{T}_i , the following finite difference equation is obtained from the one-dimensional energy equation:

$$\frac{\bar{T}_{i+1} - 2\bar{T}_i + \bar{T}_{i-1}}{(\Delta y)^2} - \frac{\eta_o}{k_s t_b} \alpha \bar{h}_i (\bar{T}_{b,i} - \bar{T}_{f,i}) = -\frac{q''}{k_s t_b} \quad (40)$$

where $\bar{T}_{b,i}$ and $\bar{T}_{f,i}$ indicate the base temperature and the bulk mean fluid temperature at the i -th control volume, respectively. Note that the bulk mean fluid temperature and the average heat transfer coefficient in the finite difference equation are coupled with the flow distribution. Therefore, n algebraic equations including the unknown values at the temperature nodes are obtained from the one-dimensional energy equation. By solving these algebraic equations simultaneously, the velocity, pressure, and temperature distributions of MMC heat sinks can be estimated. The detailed procedure for solving the one-dimensional equations is delineated in **Fig. A.3**.

References

- [1] E.M. Bibra, E. Connelly, S. Dhir, M. Drtil, P. Henriot, I. Hwang, J.-B. Le Marois, S. McBain, L. Paoli, J. Teter, *Global Ev Outlook 2022: Securing Supplies for an Electric Future*, 2022.
- [2] X. Zhang, X. Zhao, W. Li, Z. Wang, A. Liao, Y. Song, Y. Wang, L. Zhang, Ultra-thermostable embedded liquid cooling in sic 3d packaging power modules of electric vehicles, *Energy Convers. Manag.* 276 (2023) 116499, <https://doi.org/10.1016/j.enconman.2022.116499>. URL, <https://www.sciencedirect.com/science/article/pii/S0196890422012778>.
- [3] B.K. Bose, Power electronics, smart grid, and renewable energy systems, *Proc. IEEE* 105 (11) (2017) 2011–2018, <https://doi.org/10.1109/JPROC.2017.2745621>.
- [4] A. Bar-Cohen, P. Wang, E. Rahim, Thermal management of high heat flux nanoelectronic chips, *Microgravity Sci. Technol.* 19 (2007) 48–52.
- [5] A. Bar-Cohen, J.J. Maurer, J.G. Felbinger, Darpa's intra/interchip enhanced cooling (icecool) program, in: CS MANTECH Conference, May 13th–16th, 2013.
- [6] G. Moreno, K. Bennion, X. Feng, R. Kotecha, J. Major, J. Tomerlin, Power electronics thermal management (2020), URL, <https://www.osti.gov/biblio/1925167>.
- [7] E.M. Abo-Zahhad, A. Amine Hachicha, Z. Said, C. Ghenai, S. Ookawara, Thermal management system for high, dense, and compact power electronics, *Energy Convers. Manag.* 268 (2022) 115975, <https://doi.org/10.1016/j.enconman.2022.115975>. URL, <https://www.sciencedirect.com/science/article/pii/S0196890422007683>.
- [8] D. Tuckerman, R. Pease, High-performance heat sinking for vlsi, *IEEE Electron Dev. Lett.* 2 (5) (1981) 126–129, <https://doi.org/10.1109/EDL.1981.25367>.
- [9] R. Pijnenburg, R. Dekker, C. Nicole, A. Aubry, E. Eummelen, Integrated micro-channel cooling in silicon, in: *Proceedings of the 30th European Solid-State Circuits Conference (IEEE Cat. No. 04EX850)*, IEEE, 2004, pp. 129–132.
- [10] R.V. Erp, G. Kampitsis, L. Nela, R.S. Ardebili, E. Matioli, Embedded microchannel cooling for high power-density gan-on-si power integrated circuits, in: *2020 19th IEEE InterSociety Conference on Thermal and Thermomechanical Phenomena in*

- Electronic Systems (ITherm), 2020, pp. 53–59, <https://doi.org/10.1109/ITherm54881.2020.9190356>.
- [11] H. Wen, Z. Liang, Q. Luo, C. Wu, C. Wang, Heat transfer performance study of microchannel heat sink with composite secondary channels, *Int. Commun. Heat Mass Transf.* 143 (2023) 106718, <https://doi.org/10.1016/j.icheatmasstransfer.2023.106718>, <https://www.sciencedirect.com/science/article/pii/S0735193323001070>.
- [12] G. Harpole, J. Eninger, Micro-channel heat exchanger optimization, in: *Proceedings - IEEE Semiconductor Thermal and Temperature Measurement Symposium*, 1991, pp. 59–63.
- [13] D. Copeland, H. Takahira, N. Wataru, B.C. Pak, Manifold microchannel heat sinks: Theory and experiment, in: *Advances in Electronic Packaging Proc. Int. InterSociety Electronic Packaging Conference (INTERpack '95)*, 1995, pp. 829–835.
- [14] D. Copeland, M. Behnia, W. Nakayama, Manifold microchannel heat sinks: isothermal analysis, in: *InterSociety Conference on Thermal Phenomena in Electronic Systems, I-THERM V*, 1996, pp. 251–257, <https://doi.org/10.1109/ITHERM.1996.534570>.
- [15] K.W. Jung, Investigation thermo-fluidic performance of si-based embedded microchannels-3d manifold cooling system for high power density electronic applications, Ph.D. thesis, Stanford University, 2020.
- [16] E. Cetegen, Forced fed microchannel high heat flux cooling utilizing microgrooved surfaces, Ph.D. thesis, University of Maryland, College Park, 2010.
- [17] E. Kermani, Manifold micro-Channel Cooling of Photovoltaic Cells for High Efficiency Solar Energy Conversion Systems, Master's thesis, University of Maryland, College Park, 2008.
- [18] Y.J. Lee, S.J. Kim, Experimental investigation on thermal-hydraulic performance of manifold microchannel with pin-fins for ultra-high heat flux cooling, *Int. J. Heat Mass Transf.* 224 (2024) 125336, <https://doi.org/10.1016/j.ijheatmasstransfer.2024.125336>, URL, <https://www.sciencedirect.com/science/article/pii/S0017931024001674>.
- [19] R. van Erp, R. Soleimanzadeh, L. Nela, G. Kampitsis, E. Matioli, Co-designing electronics with microfluidics for more sustainable cooling, *Nature* 585 (7824) (2020) 211–216, <https://doi.org/10.1038/s41586-020-2666-1>.
- [20] W. Escher, T. Brunschwiller, B. Michel, D. Poulikakos, Experimental investigation of an ultrathin manifold microchannel heat sink for liquid-cooled chips, *J. Heat Transf.* 132 (8) (2010) 081402, <https://doi.org/10.1115/1.4001306>.
- [21] S. Wang, G. Xia, D. Ma, R. Li, L. Xu, Influence of restrictor on the thermal-hydraulic performance in manifold microchannel heat sink, *Int. Commun. Heat Mass Transf.* 149 (2023) 107093, <https://doi.org/10.1016/j.icheatmasstransfer.2023.107093>, URL, <https://www.sciencedirect.com/science/article/pii/S0735193323004827>.
- [22] J. Zhou, X. Chen, Q. Zhao, M. Lu, D. Hu, Q. Li, Flow thermohydraulic characterization of hierarchical-manifold microchannel heat sink with uniform flow distribution, *Appl. Therm. Eng.* 198 (2021) 117510, <https://doi.org/10.1016/j.applthermaleng.2021.117510>, URL, <https://www.sciencedirect.com/science/article/pii/S135943112100942X>.
- [23] X. Zhang, R. Tiwari, A.H. Shooshtari, M.M. Ohadi, An additively manufactured metallic manifold-microchannel heat exchanger for high temperature applications, *Appl. Therm. Eng.* 143 (2018) 899–908, <https://doi.org/10.1016/j.applthermaleng.2018.08.032>, URL, <https://www.sciencedirect.com/science/article/pii/S1359431118327212>.
- [24] S. Wang, H.-H. Chen, C.-L. Chen, Enhanced flow boiling in silicon nanowire-coated manifold microchannels, *Appl. Therm. Eng.* 148 (2019) 1043–1057, <https://doi.org/10.1016/j.applthermaleng.2018.11.125>, URL, <https://www.sciencedirect.com/science/article/pii/S1359431118344739>.
- [25] K. Tang, Y. Huang, G. Lin, Y. Guo, J. Huang, H. Lin, H. Zhang, Q. Yang, J. Miao, Thermal-hydraulic performance of ammonia in manifold microchannel heat sink, *Appl. Therm. Eng.* 232 (2023) 121000, <https://doi.org/10.1016/j.applthermaleng.2023.121000>, URL, <https://www.sciencedirect.com/science/article/pii/S1359431123010293>.
- [26] H. Abou-Ziyani, M. Ibrahim, H. Abdel-Hameed, Characteristics enhancement of one-section and two-stepwise microchannels for cooling high-concentration multi-junction photovoltaic cells, *Energy Convers. Manag.* 206 (2020) 112488, <https://doi.org/10.1016/j.enconman.2020.112488>, URL, <https://www.sciencedirect.com/science/article/pii/S0196890420300248>.
- [27] C. Xiao, M. Nourbakhsh, A. Alizadeh, D. Toghraie, P. Barnoon, A. Khan, Investigation of thermal behavior and performance of different microchannels: a case study for traditional and manifold microchannels, *Case Stud. Therm. Eng.* 39 (2022) 102393, <https://doi.org/10.1016/j.csite.2022.102393>, URL, <https://www.sciencedirect.com/science/article/pii/S2214157X22006293>.
- [28] K. Tang, G. Lin, Y. Guo, J. Huang, H. Zhang, J. Miao, Simulation and optimization of thermal performance in diverging/converging manifold microchannel heat sink, *Int. J. Heat Mass Transf.* 200 (2023) 123495, <https://doi.org/10.1016/j.ijheatmasstransfer.2022.123495>, URL, <https://www.sciencedirect.com/science/article/pii/S0017931022009644>.
- [29] Y.-H. Pan, R. Zhao, X.-H. Fan, Y.-L. Nian, W.-L. Cheng, Study on the effect of varying channel aspect ratio on heat transfer performance of manifold microchannel heat sink, *Int. J. Heat Mass Transf.* 163 (2020) 120461, <https://doi.org/10.1016/j.ijheatmasstransfer.2020.120461>, URL, <https://www.sciencedirect.com/science/article/pii/S0017931020333974>.
- [30] C. Chen, X. Wang, B. Yuan, W. Du, G. Xin, Investigation of flow and heat transfer performance of the manifold microchannel with different manifold arrangements, *Case Stud. Therm. Eng.* 34 (2022) 102073, <https://doi.org/10.1016/j.csite.2022.102073>, URL, <https://www.sciencedirect.com/science/article/pii/S2214157X22003197>.
- [31] C. Chen, F. Li, X. Wang, J. Zhang, G. Xin, Improvement of flow and heat transfer performance of manifold microchannel with porous fins, *Appl. Therm. Eng.* 206 (2022) 118129, <https://doi.org/10.1016/j.applthermaleng.2022.118129>, URL, <https://www.sciencedirect.com/science/article/pii/S135943112200093X>.
- [32] D. Kong, Y. Kim, M. Kang, E. Song, Y. Hong, H.S. Kim, K.J. Rah, H.G. Choi, D. Agonafer, H. Lee, A holistic approach to thermal-hydraulic design of 3D manifold microchannel heat sinks for energy-efficient cooling, *Case Stud. Therm. Eng.* 28 (2021) 101583, <https://doi.org/10.1016/j.csite.2021.101583>, URL, <https://www.sciencedirect.com/science/article/pii/S2214157X21007462>.
- [33] N. Gilmore, V. Timchenko, C. Menictas, Open manifold microchannel heat sink for high heat flux electronic cooling with a reduced pressure drop, *Int. J. Heat Mass Transf.* 163 (2020) 120395, <https://doi.org/10.1016/j.ijheatmasstransfer.2020.120395>, URL, <https://www.sciencedirect.com/science/article/pii/S0017931020333317>.
- [34] J. Yang, K. Cheng, K. Zhang, C. Huang, X. Huai, Numerical study on thermal and hydraulic performances of a hybrid manifold microchannel with bifurcations for electronics cooling, *Appl. Therm. Eng.* 232 (2023) 121099, <https://doi.org/10.1016/j.applthermaleng.2023.121099>, URL, <https://www.sciencedirect.com/science/article/pii/S1359431123011286>.
- [35] W. Xie, X. Lv, D. Liu, L. Li, W. Yao, Numerical investigation of flow boiling in manifold microchannel-based heat exchangers, *Int. J. Heat Mass Transf.* 163 (2020) 120493, <https://doi.org/10.1016/j.ijheatmasstransfer.2020.120493>, URL, <https://www.sciencedirect.com/science/article/pii/S0017931020334293>.
- [36] T. Wei, S. Hazra, Y. Lin, M.P. Gupta, M. Degner, M. Asheghi, K.E. Goodson, Numerical study of large footprint (24 x 24 mm²) silicon-based embedded microchannel three-dimensional manifold coolers, *J. Electron. Packag.* 145 (2) (2022) 021008 arXiv:https://asmedigitalcollection.asme.org/electronicpackaging/article-pdf/145/2/021008/6921258/ep_145_02_021008.pdf.
- [37] L. Boteler, N. Jankowski, P. McCluskey, B. Morgan, Numerical investigation and sensitivity analysis of manifold microchannel coolers, *Int. J. Heat Mass Transf.* 55 (2012) 7698–7708.
- [38] K.W. Jung, C.R. Kharangate, H. Lee, J. Palko, F. Zhou, M. Asheghi, E.M. Dede, K. E. Goodson, Embedded cooling with 3d manifold for vehicle power electronics application: single-phase thermal-fluid performance, *Int. J. Heat Mass Transf.* 130 (2019) 1108–1119.
- [39] M. Arie, A. Shooshtari, S. Dessiatoun, E. Al-Hajri, M. Ohadi, Numerical modeling and thermal optimization of a single-phase flow manifold-microchannel plate heat exchanger, *Int. J. Heat Mass Transf.* 81 (2015) 478–489, <https://doi.org/10.1016/j.ijheatmasstransfer.2014.10.022>, URL, <https://linkinghub.elsevier.com/retrieve/pii/S0017931014009077>.
- [40] R.A. Bajura, A model for flow distribution in manifolds, *J. Eng. Power* 93 (1971) 7–12, <https://doi.org/10.1115/1.3445410>.
- [41] J. Wang, Theory of flow distribution in manifolds, *Chem. Eng. J.* 168 (2011) 1331–1345, <https://doi.org/10.1016/j.cej.2011.02.050>.
- [42] J. Wang, Z. Gao, G. Gan, D. Wu, Analytical solution of flow coefficients for a uniformly distributed porous channel, *Chem. Eng. J.* 84 (1) (2001) 1–6, [https://doi.org/10.1016/S1385-8947\(00\)00263-1](https://doi.org/10.1016/S1385-8947(00)00263-1), URL, <https://linkinghub.elsevier.com/retrieve/pii/S1385894700002631>.
- [43] Y.S. Muzychka, M.M. Yovanovich, Laminar forced convection heat transfer in the combined entry region of non-circular ducts, *J. Heat Transf.* 126 (1) (2004) 54–61, <https://doi.org/10.1115/1.1643752>, URL, <https://asmedigitalcollection.asme.org/heattransfer/article/126/1/54/444584/Laminar-Forced-Convection-Heat-Transfer-in-the>.
- [44] Z. Duan, Y.S. Muzychka, Pressure drop of impingement air cooled plate fin heat sinks, *ASME. J. Electron. Packag.* 129 (2) (2007) 190–194.
- [45] Y. Kondo, H. Matsushima, Prediction algorithm of pressure drop for impingement cooling of heat sinks with longitudinal fins; heiban fin no funryu reikyaku ni okeru atsuryoku sonshitsu no kani yosokuho, Nippon Kikai Gakkai Ronbunshu, B Hen (Trans. Japan Soc. Mech. Eng. Part B) 61 (1995).
- [46] W. Kays, M. Crawford, Convective Heat and Mass Transfer, McGraw-Hill Series in Management, McGraw-Hill, 1980.
- [47] W. Wagner, H.-J. Kretzschmar, IAPWS Industrial Formulation 1997 for the Thermodynamic Properties of Water and Steam, Springer Berlin Heidelberg, 2008, pp. 7–150.
- [48] H.R. Shanks, P.D. Maycock, P.H. Sidles, G.C. Danielson, Thermal conductivity of silicon from 300 to 1400°K, *Phys. Rev.* 130 (1963) 1743–1748, <https://doi.org/10.1103/PhysRev.130.1743>, URL, <https://link.aps.org/doi/10.1103/PhysRev.130.1743>.
- [49] S. Sarangi, K.K. Bodla, S.V. Garimella, J.Y. Murthy, Manifold microchannel heat sink design using optimization under uncertainty, *Int. J. Heat Mass Transf.* 69 (2014) 92–105.
- [50] W. Escher, B. Michel, D. Poulikakos, A novel high performance, ultra thin heat sink for electronics, *Int. J. Heat Fluid Flow* 31 (4) (2010) 586–598, <https://doi.org/10.1016/j.ijheatfluidflow.2010.03.001>.
- [51] S.U. Yuruker, R.K. Mandel, A. Shooshtari, M.M. Ohadi, A metamodeling approach for optimization of manifold microchannel systems for high heat flux cooling applications, in: 2019 18th IEEE Intersociety Conference on Thermal and Thermomechanical Phenomena in Electronic Systems (ITherm), 2019, pp. 982–990, <https://doi.org/10.1109/ITHERM.2019.8757232>.
- [52] C.N.P.G. Arachchige, L.A. Prendergast, R.G. Staudte, Robust analogs to the coefficient of variation, *J. Appl. Stat.* 49 (2) (2022) 268–290, <https://doi.org/10.1080/02664763.2020.1808599>, URL, <https://www.tandfonline.com/doi/full/10.1080/02664763.2020.1808599>.